Deriving Fermi arcs of generic nature spanning nodes featuring multibands, nonlinear dispersion, and/or multipoles

Ipsita Mandal
Department of Physics, Shiv Nadar Institution of Eminence (SNIoE), Gautam Buddha Nagar, Uttar Pradesh 201314, India

Fermi arcs appear as the surface states at the boundary of a three-dimensional topological semimetal with the vacuum, reflecting the Chern number ($\mathcal{C}$) of a nodal point in the momentum space, which represents singularities (in the form of monopoles) of the Berry curvature. They are finite arcs (rather than closed curves), attaching/reattaching with the bulk-energy states at the tangents of the projections of the Fermi surfaces of the bands meeting at the nodes. The number of Fermi arcs grazing onto the tangents of the outermost projection equals $\mathcal{C}$, revealing the intrinsic topology of the underlying bandstructure, which can be visualised in experiments like ARPES. Here we outline a generic procedure to compute these states for generic nodal points, (1) whose degeneracy might be twofold or multifold; and (2) the associated bands might exhibit isotropic or anisotropic, linear- or nonlinear-in-momentum dispersion. This also allows us to determine whether we should get any Fermi arcs at all for $\mathcal{C} = 0$, when the nodes host ideal dipoles.

Introduction.— Nodal points (NPs) in three-dimensional (3d) semimetals represent defective points in the Brillouin zone (BZ), where $(2\varsigma+1)$ cross at a nodal-point degeneracy [see Fig. 3(a)]. In the vicinity of a nodal point, the bands form a spin-ς representation of the SU(2) group. They provide an intriguing crucible to observe mathematical notions of topology playing out in real-life systems [1–6] because they are the singular points of the Berry-curvature (BC) where it blows up, hosting a BC-monopole synonymous with the net Chern number ($\mathcal{C}$) at the NP. An isotropic Weyl node, appearing in semimetals (WSMs) [1, 2], carrying $\varsigma = 1/2$, is the poster child of such systems, depicting the simplest scenario. The ubiquitousness of the NPs is reflected by WSMs' multifold cousins like the triple-point semimetals (with $\varsigma = 1$) and Rarita-Schwinger-Weyl (RSW) nodes (with $\varsigma = 3/2$) [4, 5, 7–12]. The singularity of the BC at an NP [13] goes beyond the monopole-character, as the possibility of ideal BC-dipoles and higher-order poles have been predicted [14–16], when considering a multipole expansion of the Berry connection [cf. Fig. 3(b)].

Often our study of the intrinsic topology of the 3d BZ, when treated as a 3d manifold, involves identifying unambigous quantitative signatures of the topological invariants like $\mathcal{C}$. Arguably Fermi arcs provide the most undisputed observables [17–24], as contemporary experiments like angle-resolved photoemission spectroscopy (ARPES) can clearly visualise them. Physically, they emerge as the locii of the surface edge-states when we take a surface (say, whose outward normal is along the normal is along the unit vector, $\hat{\boldsymbol{n}}$) of a slab of a topological semimetal. In fact, these surface states arise due to the presence of chiral edge modes in 2d slices of the 3d BZ, after we impose open boundary conditions on those slices [1, 2]. Although we can no longer describe the system in the momentum space for the direction along $\hat{\boldsymbol{n}}$, the momentum-components perpendicular-to-$\hat{\boldsymbol{n}}$ (say, $\mathbf{k}_\parallel$), i.e., parallel to the surface itself, remain good quantum numbers (as long as we consider very large spatial dimensions along those directions). Thus, a single (boundary) surface in real space gives us an SBZ, spanned by the components of $\mathbf{k}_\parallel$, and hosting the Fermi arcs. Although the analytical derivation of surface states, which take the form of Fermi arcs in NPs, is well-understood for the case of Weyl semimetals [25–28], for most other cases, the derivations are system-specific and not generic-enough [25, 29–33] to be applicable for arbitrary cases of dispersion (for example, anisotropic and/or nonlinear-in-momentum behaviour) and band-crossings. In this Letter, our aim is to outline a generic procedure to obtain the analytical forms of the Fermi arcs and demonstrate its effectiveness by applying it to a variety of NPs.

Surface Hamiltonian.— Let us take a single surface at $x = 0$ such that the $x < 0$ region represent a semi-infinite semimetal, with the bulk Hamiltonian $H(\mathbf{k})$, where $\mathbf{k} \equiv \{k_x, k_y, k_z\}$ and $k = \sqrt{k_x^2 + k_y^2 + k_z^2}$. The translation symmetry is broken along the x-axis, and we use the Hamiltonian, $H_x = H(k_x \to -i\,\partial_x, k_y, k_z)$. Demanding that H_x be Hermitian in the region $x \in [0, \infty)$, we have the physical condition that

$$\int_0^\infty dx\, \psi^\dagger(x)\, H_x\, \phi(x) = \int_0^\infty dx\, [H_x\, \psi(x)]^\dagger\, \phi(x)\,, \qquad (1)$$

while considering two bonafide boundary-states, ψ and ϕ. The current-density operator is defined as $j_x \equiv \partial_{k_x} H(\mathbf{k})|_{k_x \to -i\,\partial_x}$. Consequently, Eq. (1) also translates into a physically-sensible boundary condition which prohibits the current transmission through the boundary via $(\psi^\dagger\, j_x\, \psi)|_{x=0} = 0$, alternatively known as the hard-wall bc. The boundary modes must behave as decaying wavefunctions of the form of $\psi(x) = \psi_0\, e^{-\kappa\, x}$ with $\mathrm{Re}(\kappa) > 0$, so that the surface states are bound to the boundary at $x = 0$. Here, ψ_0 is independent of x and any x-dependence of $\psi(x)$ is assumed to be contained in the $e^{-\kappa\, x}$ factor.

Witten's formulation for an untilted Weyl node.— The effective Hamiltonian in the vicinity of a single Weyl node [cf. Fig. 3(a)] is captured by

$$H_W(\mathbf{k}) = \boldsymbol{\sigma} \cdot \mathbf{k}\,, \qquad (2)$$

for which Eq. (1) translates into $\psi^\dagger(x)\, \sigma_x\, \phi(x)|_{x=0} = 0 \Rightarrow j_x|_{x=0} \equiv \psi_0^\dagger\, \sigma_x\, \phi_0 = 0$. Witten [25] prescribed an energy-independent boundary condition,

$$\Psi_0 = M\, \Psi_0\,, \text{ where } M = \cos\alpha\, \sigma_y + \sin\alpha\, \sigma_z\,, \qquad (3)$$

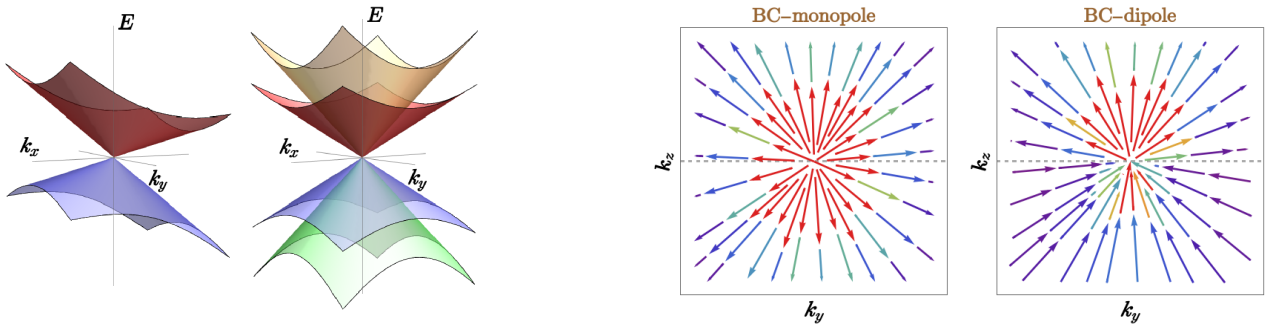

(a) (b)

FIG. 1. (a) Dispersion (E) in tilted Weyl node and fourfold (viz. Rarita-Schwinger-Weyl node) band-crossings against the k_xk_y-plane. (b) Schematics of BC-flux lines in the $k_x = 0$ planes for a monopole and an ideal dipole.

as a local linear restriction on the components of the spinor wave function. This is a good boundary condition because σ_x anticommutes with M, leading to $\psi_0^\dagger \sigma_x \phi_0 = \frac{1}{2}\left[\psi_0^\dagger \sigma_x M \phi_0 + (M\psi_0)^\dagger \sigma_x \phi_0\right] = 0$. By changing the parameter α, we get Fermi arcs of various shapes and orientations with the restriction that they originate tangentially from the boundary of the projection of the FS on the k_yk_z-plane.

Generic formulation.— For generic nodes with multifold nodes and/or nonlinear powers of the components of $\mathbf{k}$, Witten's trick will not work, which we will explicitly see why considering some specific examples. Hence, we need an unambigous generic method applicable to derive the equations describing the curves representing the relevant Fermi arcs, which we describe here. Suppose we have an N-fold degeneracy at a node, described by the $N \times N$ Hamiltonian, $H_N(\mathbf{k})$ in the bulk BZ. Let us look for surface states where the surface-normal is along the direction denoted by the unit vector, $\hat{\boldsymbol{n}}$, and located at $r_\perp = 0$, where $r_\perp \equiv \mathbf{r}\cdot\hat{\boldsymbol{n}}$. We set our convention that the region $r_\perp < 0$ represents the region occupied by the semimetallic material, while $r_\perp > 0$ represents the adjoining non-topological region (e.g., vacuum). Dividing up the momentum components along and perpendicular to $\hat{\boldsymbol{n}}$ as $k_\perp$ and $\mathbf{k}_\parallel$, the boundary Hamiltonian is obtained as $H_{r_\perp} = H_N(k_\perp \to -i\,\partial_{r_\perp}, \mathbf{k}_\parallel)$. The imposition of the Hermiticity condition on $H_{r_\perp}$ leads to

$$\int_0^\infty dr_\perp\, \psi^\dagger(r_\perp)\, H_{r_\perp}\, \phi(r_\perp) = \int_0^\infty dr_\perp\, [H_{r_\perp}\, \psi(r_\perp)]^\dagger\, \phi(r_\perp)\,, \tag{4}$$

analogous to Eq. (1). Let us parametrise a solution as

$$\psi(r_\perp) = \psi_0\, e^{-\kappa\, r_\perp} \text{ with } \mathrm{Re}(\kappa) > 0 \text{ and}$$
$$\psi_0^T = \left[1 \;\; a_1 + i\,b_1 \;\; a_2 + i\,b_2 \;\; \cdots \;\; a_{N-1} + i\,b_{N-1}\right]. \tag{5}$$

As argued earlier, (after some manipulations involving integration by parts to convert the integrands into total derivatives) Eq. (4) will turn out to be equivalent to the condition of

$$\psi^\dagger(r_\perp)\, j_{r_\perp}\psi(r_\perp)\big|_{r_\perp=0} = 0\,, \text{ where}$$
$$j_{r_\perp} \equiv \partial_{k_\perp} H_N(k_\perp, \mathbf{k}_\parallel)\big|_{k_\perp \to -i\,\partial_{r_\perp}} \tag{6}$$

represents the current-density operator perpendicular to the surface. Next, we need to solve for the eigenvalue equation,

$$H_{r_\perp}\psi(r_\perp) = E\,\psi(r_\perp)\,, \tag{7}$$

which leads to N complex-valued equations involving the $(2N+1)$ unknown variables E, $\kappa_r \equiv \mathrm{Re}(\kappa)$, $\kappa_i \equiv \mathrm{Im}(\kappa)$, a_1, b_1, a_2, b_2, $\cdots$, a_{N-1}, and b_{N-1}. This implies that we have $(2N+1)$ real equations [on including the real equation coming from Eq. (6)] at our disposal, which we can use to solve for the same number of unknown variables. In the next section, we will study a variety of systems to see that the above procedure works generically.

Weyl nodes.— Let us consider the one-node model given by Eq. (2), where we want to consider a boundary at $x = 0$, indicating $\hat{\boldsymbol{n}} = \hat{\boldsymbol{x}}$. Using $\psi_0^T = \left[1 \;\; a_1 + i\,b_1\right]$, we get $E = \frac{2\,b_1\,k_y + (1-b_1^2)\,k_z}{1+b_1^2}$, $\kappa_r = \frac{(b_1^2-1)k_y + 2\,b_1\,k_z}{1+b_1^2}$, and $\kappa_i = 0$. We find that b_1 plays the role of a parameter, just like α in Eq. (3). The range of the Fermi arc is determined by the region where $\kappa_r > 0$, i.e., $\left(b_1^2 - 1\right)k_y + 2\,b_1\,k_z > 0$. The arcs end tangentially on the projections of the bulk FSs, mixing with the bulk states, which is the point where k_y and k_z are as the solutions of the simultaneous equations, $E(k_y, k_z) = \mu$ and $\sqrt{k_y^2 + k_z^2} = \mu$. One can check that at this point, $\{k_y, k_z\} = \frac{\mu}{1+b_1^2}\{2\,b_1,\, 1 - b_1^2\} \Rightarrow \kappa_r = 0$. Therefore, the surface state ceases to exist at this point, merging with the bulk states.

Tilted Weyl nodes.— The bulk Hamiltonian in the vicinity of a node, tilted with respect to the k_x-axis, is captured by $H_W(\mathbf{k}) = \boldsymbol{\sigma}\cdot\mathbf{k} + \eta\,k_x\,\mathbb{I}_{2\times2}$. For this case, on using $\psi_0^T = \left[1 \;\; a_1 + i\,b_1\right]$, we obtain the solutions as $E = \frac{b_1\left[\sqrt{1-\left(1+b_1^2\right)\eta^2}+1\right]k_y + \left[\sqrt{1-\left(1+b_1^2\right)\eta^2}-b_1^2\right]k_z}{1+b_1^2}$, $\kappa_r = \frac{\left(b_1^2-1\right)k_y + 2\,b_1\,k_z}{1+b_1^2}$, $\kappa_i = 0$, and $a_1 = \frac{\sqrt{1-\left(1+b_1^2\right)\eta^2}-1}{\eta}$. While for the untilted case (i.e., $\eta = 0$), the projection is the locus of the curve $k = \mu$ at $k_x = 0$, for the tilted case (i.e., $\eta \neq 0$), it is the locus of the curve $k = \mu$ at $k_x = -\eta\sqrt{(k_y^2 + k_z^2)/(1-\eta^2)}$. This is because, for $\mu \neq 0$, the anisotropic FS (shaped as a spheroid elongated along

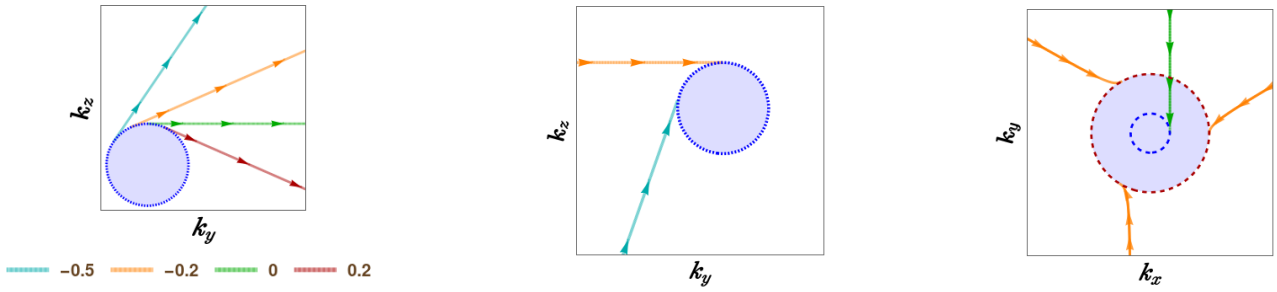

(a) (b) (c)

FIG. 2. (a) Tilted Weyl node with $\eta = 0.35$: Each Fermi arc corresponds to a distinct value of b_1, colour-coded as shown in the plot-legends. (b) TSM node: 2 Fermi arcs entering into FS-projection, representing $\mathcal{C} = -2$. (c) RSW node: 4 Fermi arcs entering into the FS-projections, representing $\mathcal{C} = -3$. The dashed circles represent the projections of the bulk FSs with $\mu = 0.5$.

the k_x-direction) has its largest radius-of-projection at a negative value of k_x. Fig. 2(a) illustrates the Fermi arcs for four distinct values of b_1, with η set to 0.35.

Pseudospin-1 nodes.— Let us now consider bands carrying pseudospin-1 quantum numbers crossing at threefold-degenerate nodes [4, 5, 34–36], representing the so-called triple-point semimetals (TSMs). These are three-band generalisations of the pseudospin-1/2 quasiparticles in Weyl semimetals, with the nodal points acting as Berry-curvature monopoles of magnitude 2. They can be realised in 3d tight-binding models for cold fermionic atoms in cubic optical lattices [37] and, via *ab initio* simulations, have been identified in materials like TaN, NbN, and WC-type ZrTe [34, 38–40]. The effective low-energy continuum Hamiltonian, in the vicinity of a threefold nodal point, is given by $\mathcal{H}_T(\mathbf{k}) = \mathbf{k}\cdot\boldsymbol{\mathcal{S}}$, where $\boldsymbol{\mathcal{S}}$ represents the vector spin-1 operator with three components [36]. The Chern-number values of ± 2 indicate that we must have two distinct Fermi arcs associated with each node [20, 21]. Here we note that, although this is a straightforward generalisation of the isotropic Weyl node, we cannot apply Witten's method simply because of the fact that $\mathcal{S}_x$, $\mathcal{S}_y$, and $\mathcal{S}_z$ *do not anticommute* (unlike the Pauli matrices). For the same reason, the boundary-condition matching procedure of Ref. [41] is inadequate and non-generic for dealing with this system. Hence, our generic method is indispensable to explicitly derive the appearances of the Fermi arcs. We use the parametrisation $\psi_0^T = \begin{bmatrix}1 & a_1 + i\,b_1 & a_2 + i\,b_2\end{bmatrix}$ and consider a boundary at $x = 0$. Plugging it in Eqs. (6) and Eq. (7), the solutions indeed tell us that there are two Fermi arcs characterised by (1) $E = \frac{2\sqrt{2}\,b_1\,k_y + 4\,k_z}{2+b_1^2} - k_z$, $\kappa_r = \frac{(b_1^2-2)k_y + 2\sqrt{2}\,b_1\,k_z}{2+b_1^2}$, $\kappa_i = 0$, $a_1 = 0$, $a_2 = -\,b_1^2/2$, $|b_1| > 0$, and $b_2 = 0$; and (2) $E = k_z$, $\kappa_r = -\,k_y$, $\kappa_i = 0$, $a_1 = 0$, $a_2 = 0$, $b_1 = 0$, and $b_2 = 0$. For the first arc, b_1 plays the role of a parameter and, hence, its shape changes as we vary b_1. Fig. 2(b) illustrates the Fermi arcs for $\mu = 0.5$ and $b_1 = -1$. Since $|\mathcal{C}| = 2$, we observe two arcs entering into the FS-projection.

Rarita-Schwinger-Weyl node.— Here we focus on bands carrying pseudospin-3/2 quantum numbers crossing at fourfold-degenerate degenracy-points [cf. Fig. 3(a)], widely known as the Rarita-Schwinger-Weyl (RSW) nodes. They appear at the Γ-points of chiral crystals with appreciable SOC couplings [5, 12, 22, 36, 42], hosting a net BC-monopole of magnitude 4. The effective Hamiltonian, in the vicinity of an isotropic RSW node, takes the form of $\mathcal{H}(\boldsymbol{k}) = \mathbf{k}\cdot\boldsymbol{\mathcal{J}}$, where $\boldsymbol{\mathcal{J}} = \{\mathcal{J}_x, \mathcal{J}_y, \mathcal{J}_z\}$ represents the vector operator whose three components comprise the angular-momentum operators in the spin-3/2 representation of the SU(2) group. Since the RSW node carries $\mathcal{C} = 4$, we must observe four arcs emanating from the FS-projections of the two nodes being cut by μ. For this case, just for the ease of calculations, we consider a boundary at $z = 0$ (just because the $\mathcal{J}$ matrix has fewer nonzero entries, leading to less cumbersome equations to be solved). Here again we note that, although this is a fourfold generalisation of the isotropic Weyl node, we cannot apply Witten's method since $\mathcal{J}_x$, $\mathcal{J}_y$, and $\mathcal{J}_z$ *do not anticommute* (unlike the Pauli matrices). Hence, we need to utilise our generic method to explicitly derive the equations of the Fermi arcs. We use the parametrisation $\psi_0^T = \begin{bmatrix}1 & a_1 + i\,b_1 & a_2 + i\,b_2 & a_3 + i\,b_3\end{bmatrix}$ because of the fourfold nature of the bands. Plugging it Eqs. (6) and Eq. (7) yield the explicit solutions which are long and cumbersome and can be parametrised in terms of one free parameter (which could be any of the $\{a_1, a_2, a_3, b_1, b_2, b_3\}$). Hence, we do not write those explicitly. Instead, in Fig. 2(c), we demonstrate four Fermi arcs entering into the projection of the outer FS.

Double-Weyl nodes.— Double-Weyl nodes can be found in materials like $HgCr_2Se_4$ [43] and $SrSi_2$ [44, 45]), which exhibits a hybrid of linear dispersion (chosen to be the k_z-axis) and quadratic dispersion (in the k_xk_y-plane). In the vicinity of such a nodal point, the low-energy effective continuum Hamiltonian is given by [4, 46–49] $H_{dW} = \boldsymbol{d}\cdot\boldsymbol{\sigma}$, where $\boldsymbol{d} \equiv \{d_x, d_y, d_z\} = \{k_x^2 - k_y^2,\, 2\,k_x\,k_y,\, k_z\}$. Plugging in the parametrisation of $\psi_0^T = \begin{bmatrix}1 & a_1 + i\,b_1\end{bmatrix}$ in Eq. (6) leads to: $E = \frac{\sqrt{k_z^2\cos^2 t - 4\,k_y^4\tan^2 t}}{\cos t}$, $\kappa_r = \frac{s\,k_y}{\cos(t)}$, , where $a = s\,\frac{k_z\,\cos t - \sqrt{k_z^2\cos^2 t - 4\,k_y^4\tan^2 t}}{2\,k_y^2\left(1+\frac{1}{\cos t}\right)}$ and $s = \pm 1$, where $a_1 = a\cos t$ and $b_1 = a\sin t$. Thus, t serves an undetermined parameter, producing curves of varying shapes. The points on the SBZ where κ_r goes to zero are found to be $\{k_y, k_z\} = \{0, \pm\mu\}$. Fig. 3(a) illustrates the Fermi arcs for $\mu = 0.5$ and $t = \pi/6$. Since $\mathcal{C} = 2$, we observe two arcs emanating from the perimeter of the FS-projection.

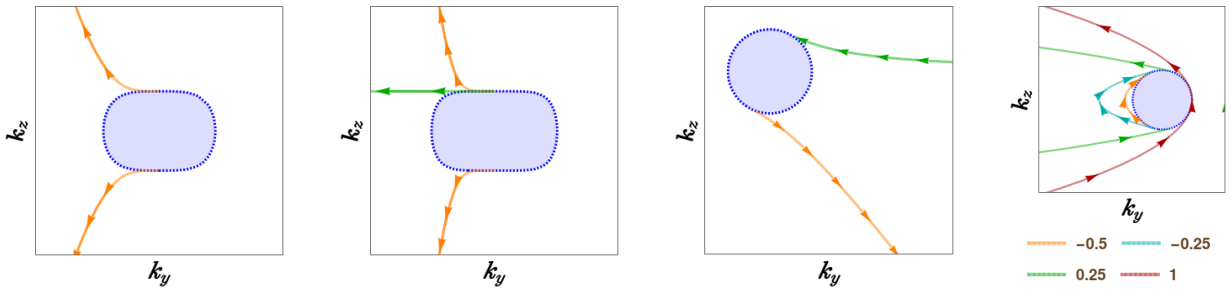

FIG. 3. (a) Double-Weyl node: 2 Fermi arcs leaving from the FS-projection, representing $\mathcal{C} = 2$. (b) Triple-Weyl node: 3 Fermi arcs leaving from the FS-projection, representing $\mathcal{C} = 3$. (c) and (d) represent the models with BC-dipole with two and three bands, respectively. For each of them, 2 counterpropagating Fermi arcs are seen – one leaving and the other entering the FS-projection. The dashed blue circles represent the projections of the bulk FSs on the $k_y k_z$-plane and $\mu = 0.5$ for each case. In subfigure (d), arcs for 4 distinct values of b_1 have been shown.

Triple-Weyl nodes.— Analogous to the double-Weyl nodes, there exist triple-Weyl nodes (in materials like transition-metal monochalcogenides [50]) from which bands with anisotropic dispersion emerge. The triple-Weyl case comprises a hybrid of linear dispersion (chosen to be the k_z-axis) and quadratic dispersion (in the $k_x k_y$-plane). In the vicinity of such a nodal point, the low-energy effective continuum Hamiltonian is given by [4, 46–48, 50] $H_{tW} = \boldsymbol{d}\cdot\boldsymbol{\sigma}$, where $\boldsymbol{d} \equiv \{d_x, d_y, d_z\} = \{k_x^3 - 3\,k_x\,k_y^2,\, 3\,k_x^2\,k_y - k_y^3\}$. Plugging in the parametrisation of $\psi_0^T = \begin{bmatrix}1 & a_1 + i\,b_1\end{bmatrix}$ leads to the required equations. Finding exact analytical solutions is cumbersome because of the cubit roots involved. Instead, we parametrise $a_1 = a\cos t$ and $b_1 = \sin t$, and we show below the solutions for $t = 0$: (1) $E = k_z$, $\kappa_r = \pm\,k_y$, $\kappa_i = 0$, and $a = 0$; (2) $E = \frac{1}{3}\sqrt{9\,k_z^2 - \frac{512\,k_y^6}{3}}$, $\kappa_r = s\,k_y$, $\kappa^2 = \tilde{s}\,\frac{2\,k_y}{\sqrt{3}}$, and $a = s\,\tilde{s}\,\frac{3\sqrt{3}\,k_z - \sqrt{27\,k_z^2 - 512\,k_y^6}}{64\,k_y^3}$, where $(s, \tilde{s}) = \pm 1$. Fig. 3(b) illustrates the Fermi arcs for $\mu = 0.5$ and $s = 1$ (the value of $\tilde{s}$ does not matter) for the solution detailed above. Since the nodes carry $\mathcal{C} = 3$, we observe three arcs emanating from the perimeter of the FS-projection.

Berry-dipole in a two-band model.— In a specific two-band model, the low-energy effective Hamiltonian in the vicinity of a single node harbouring a Berry-dipole [cf. Fig. 3(b)] is captured by [14] $H_{bd}(k_x, k_y, k_z) = 2\,v\,v_z\,q_z\,(q_x\,\sigma_x + q_y\,\sigma_y) + \left[v^2\left(q_x^2 + q_y^2\right) - q_z^2\right]\sigma_z$. Since this is a two-band model, we again use $\psi_0^T = \begin{bmatrix}1 & a_1 + i\,b_1\end{bmatrix}$. We obtain the solutions as $E = \frac{k_z\,v_z}{b_1^2}\left[2\,b_1\,v_p\,k_y + \left(b_1^2 - 1\right)k_z\,v_z\right]$, $\kappa_r = k_y - \frac{k_z v_z}{b_1 v_p}$, $\kappa_i = 0$, and $a_1 = 0$. The points on the SBZ where κ_r goes to zero are antipodal points, whose tangents are $\propto \pm\{b_1, -1\}$. This shows one arc is leaving and another is entering into the bulk states which are located at the two hemispheres of the FS and which yield ± 1 on integrating the BC-flux on their surfaces. This reflects the intrinctic dipole-character with $\mathcal{C} = 0$. Thus, Fermi arcs do arise as surface states, representing edge states on 2d slices carrying opposite Chern numbers, ± 1. Fig. 3(c) illustrates the scenario.

Berry-dipole in a three-band model.— In Ref. [15], massless multifold Hopf semimetals have been introduced which host BC-dipoles at nodes where linearly-dispersing bands cross. We consider the simplest case with threefold-degenerate node, captured by the effective continuum Hamiltonian [15, 16], $H_H = k_x\,\lambda_1 + k_y\,\lambda_2 + k_z\,\lambda_5$, where

$$\lambda_1 = \begin{bmatrix}0 & 1 & 0\\ 1 & 0 & 0\\ 0 & 0 & 0\end{bmatrix}, \quad \lambda_2 = \begin{bmatrix}0 & -i & 0\\ i & 0 & 0\\ 0 & 0 & 0\end{bmatrix}, \quad \lambda_5 = \begin{bmatrix}0 & 0 & -i\\ 0 & 0 & 0\\ i & 0 & 0\end{bmatrix}.$$

For this 3-band model, we use the parametrisation $\psi_0^T = \begin{bmatrix}1 & a_1 + i\,b_1 & a_2 + i\,b_2\end{bmatrix}$. The solutions turn out to be $E = \frac{b_1\,k_y + \sqrt{b_1^2\left(k_y^2 + k_z^2\right) + k_z^2}}{1 + b_1^2}$, $\kappa_r = \frac{k_z^2 + b_1\sqrt{b_1^2\left(k_y^2 + k_z^2\right)} - k_y}{1 + b_1^2}$, $\kappa_i = 0$, $a_2 = 0$, and $b_2 = \frac{\sqrt{b_1^2\left(k_y^2 + k_z^2\right) + k_z^2} - b_1 k_y}{k_z}$. The points on the SBZ where κ_r goes to zero have the tangents are proportional to $\{\pm\sqrt{1 - b_1^2},\, -b_1\}$, which again leads to the picture that one arc is entering and the other leaving the bulk-states. This observation is tied to the fact that these two points are associated with 2d slices, when exclusively containing odd number of the resulting edge-modes, carry opposite Chern numbers. Of course their net Chern number is zero when they contain zero, two, or four edge-modes. Fig. 3(d) demonstrates the nature of the Fermi arcs for some distinct values of b_1.

Quadruple-Weyl node.— A quadruple-Weyl node (QWN) with twofold degeneracy carries $\mathcal{C} = 4$ [51–54] and can exist only in spinless systems at specific time-reversal symmetric points. Thus, they can appear in electronic bandstructures of materials with negligible SOC-couplings or in the phonon spectra of artificial crystals (such as photonic crystals), all of which can be treated as spinless systems. Let us take the lattice model of Ref. [54], where two nodes of opposite chiralities emerge at the Γ- and R-points. For the node sitting at the Γ-point can be described by the Hamiltonian, $H_{qW} = \boldsymbol{d}\cdot\boldsymbol{\sigma}$, where $\boldsymbol{d} \equiv \{d_x, d_y, d_z\} = \left\{\frac{v\left(k_x^2 - k_y^2\right)}{2},\, \frac{\left(k_x^2 + k_y^2 - 2\,k_z^2\right)}{2},\, v\,k_x\,k_y\,k_z\right\}$. Here we fix v to be positive. The energy eigenvalues are given by $\pm\sqrt{v^2\left[2\,k_x^2\,k_y^2\left(2\,k_z^2 - 1\right) + k_x^4 + k_y^4\right] + \left(k_x^2 + k_y^2 - 2\,k_z^2\right)^2}/2$. Clearly, the dispersion of the bands are anisotropic, with

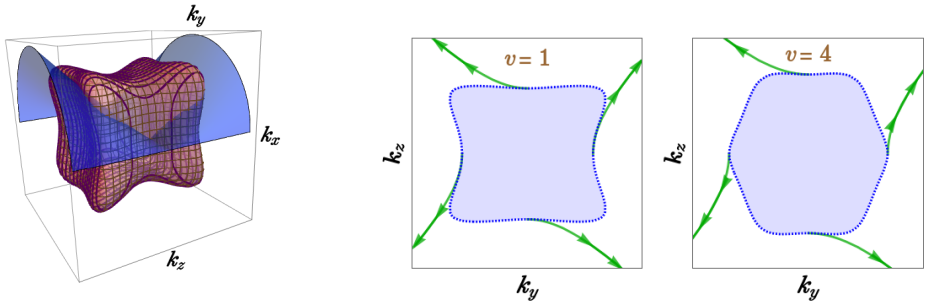

(a) (b)

FIG. 4. (a) The FS-projection is obtained by cutting the 3d FS with the yellow-coloured 2d surface. Here, $\mu = 0.25$ and $v = 1$. (b) The Fermi arcs represent modes with $E = 0.25$, emanating from the FS-projection (dashed closed curve) on the $k_y k_z$-plane.

a cubic dispersion along the (111) direction and quadratic dispersion along any other direction. Here, we expect 4 Fermi arcs to emanate from the nodal point [24], which we will derive explicitly by considering a boundary at $x = 0$. On using $\psi_0^T = \begin{bmatrix} 1 & a_1 + i\, b_1 \end{bmatrix}$, Eq. (6) yields the admissible solutions for $\mu \geq 0$ are: (1) $E = -\frac{v\left(k_y^2 - k_z^2\right)}{\sqrt{1+v^2}}$, $\kappa_r = -k_y\, k_z$, $\kappa_i = \pm\sqrt{\frac{2\,k_z^2 - k_y^2[v^2(k_z^2-1)+1]}{1+v^2}}$, $a_1 = \frac{1}{\sqrt{v^2+1}}$, and $b_1 = \frac{-v}{\sqrt{v^2+1}}$; and (2) $E = \frac{v\left(k_y^2 - k_z^2\right)}{\sqrt{1+v^2}}$, $\kappa_r = k_y\, k_z$, $\kappa_i = \pm\sqrt{\frac{2\,k_z^2 - k_y^2[v^2(k_z^2-1)+1]}{1+v^2}}$, $a_1 = \frac{-1}{\sqrt{v^2+1}}$, and $b_1 = \frac{v}{\sqrt{v^2+1}}$. The points on the SBZ where κ_r goes to zero have the tangents proportional to $\{\pm 1, 0\}$ and $\{0, \pm 1\}$. Fig. 4 illustrates a Fermi surface in 3d BZ as well as the arcs in the SBZ for $\mu = 0.25$, reflecting $\mathcal{C} = 4$.

Conclusion.— We have outlined how one can generically compute surface states in 3d topological semimetals. Through explicit examples, we have shown how the Fermi arc(s) reflect the net Chern number at a given NP, conforming to the well-established notion of bulk-boundary correspondence. Immediate future directions involve deciphering the dynamics of the Frmi arcs in the unconventional NPs studied here, which include nature of quantum oscillations [55].

[1] A. A. Burkov and L. Balents, Phys. Rev. Lett. **107**, 127205 (2011); P. Hosur, Phys. Rev. B **86**, 195102 (2012).

[2] N. P. Armitage, E. J. Mele, and A. Vishwanath, Rev. Mod. Phys. **90**, 015001 (2018); P. Hosur and X. Qi, Comptes Rendus Physique **14**, 857 (2013); B. Yan and C. Felser, Annual Rev. of Condensed Matter Phys. **8**, 337 (2017).

[3] I. Mandal and K. Saha, Ann. Phys. (Berlin) **536**, 2400016 (2024).

[4] B. Bradlyn, J. Cano, Z. Wang, M. G. Vergniory, C. Felser, R. J. Cava, and B. A. Bernevig, Science **353** (2016); C. Fang, M. J. Gilbert, X. Dai, and B. A. Bernevig, Phys. Rev. Lett. **108**, 266802 (2012).

[5] F. Flicker, F. de Juan, B. Bradlyn, T. Morimoto, M. G. Vergniory, and A. G. Grushin, Phys. Rev. B **98**, 155145 (2018).

[6] F. Balduini, A. Molinari, L. Rocchino, V. Hasse, C. Felser, M. Sousa, C. Zota, H. Schmid, A. G. Grushin, and B. Gotsmann, Nature Communications **15**, 6526 (2024).

[7] L. Liang and Y. Yu, Phys. Rev. B **93**, 045113 (2016).

[8] H. Isobe and L. Fu, Phys. Rev. B **93**, 241113 (2016).

[9] P. Tang, Q. Zhou, and S.-C. Zhang, Phys. Rev. Lett. **119**, 206402 (2017).

[10] J.-Z. Ma, Q.-S. Wu, M. Song, S.-N. Zhang, E. Guedes, S. Ekahana, M. Krivenkov, M. Yao, S.-Y. Gao, W.-H. Fan, *et al.*, Nature Communications **12**, 3994 (2021).

[11] Y. Shen, Y. Jin, Y. Ge, M. Chen, and Z. Zhu, Phys. Rev. B **108**, 035428 (2023).

[12] R. Ghosh, F. Haidar, and I. Mandal, Phys. Rev. B **110**, 245113 (2024); I. Mandal, S. Saha, and R. Ghosh, Solid State Communications **397**, 115799 (2025); I. Mandal, arXiv e-prints (2025), arXiv:2506.12380 [cond-mat.mes-hall].

[13] D. Xiao, M.-C. Chang, and Q. Niu, Rev. Mod. Phys. **82**, 1959 (2010); G. Sundaram and Q. Niu, Phys. Rev. B **59**, 14915 (1999); A. Graf and F. Piéchon, Phys. Rev. B **104**, 085114 (2021).

[14] Z.-Y. Zhuang, C. Zhang, X.-J. Wang, and Z. Yan, Phys. Rev. B **110**, L121122 (2024).

[15] A. Graf and F. Piéchon, Phys. Rev. B **108**, 115105 (2023).

[16] T. Habe, Phys. Rev. B **106**, 205204 (2022); S. Ahn, Journal of the Korean Physical Society **84**, 59 (2024).

[17] S.-Y. Xu, I. Belopolski, N. Alidoust, M. Neupane, G. Bian, C. Zhang, R. Sankar, G. Chang, Z. Yuan, C.-C. Lee, S.-M. Huang, H. Zheng, J. Ma, D. S. Sanchez, B. Wang, A. Bansil, F. Chou, P. P. Shibayev, H. Lin, S. Jia, and M. Z. Hasan, Science **349**, 613 (2015).

[18] B. Q. Lv, H. M. Weng, B. B. Fu, X. P. Wang, H. Miao, J. Ma, P. Richard, X. C. Huang, L. X. Zhao, G. F. Chen, Z. Fang, X. Dai, T. Qian, and H. Ding, Phys. Rev. X **5**, 031013 (2015).

[19] D. S. Sanchez, I. Belopolski, T. A. Cochran, X. Xu, J.-X. Yin, G. Chang, W. Xie, K. Manna, V. Süß, C.-Y. Huang, N. Alidoust, D. Multer, S. S. Zhang, N. Shumiya, X. Wang, G.-Q. Wang, T.-R. Chang, C. Felser, S.-Y. Xu, S. Jia, H. Lin, and M. Zahid Hasan, Nature **567**, 500–505 (2019).

[20] D. Takane, Z. Wang, S. Souma, K. Nakayama, T. Nakamura, H. Oinuma, Y. Nakata, H. Iwasawa, C. Cacho, T. Kim, K. Horiba, H. Kumigashira, T. Takahashi, Y. Ando, and T. Sato, Phys. Rev. Lett. **122**, 076402 (2019).

[21] N. B. M. Schröter, S. Stolz, K. Manna, F. de Juan, M. G. Vergniory, J. A. Krieger, D. Pei, T. Schmitt, P. Dudin, T. K. Kim, C. Cacho, B. Bradlyn, H. Borrmann, M. Schmidt, R. Widmer, V. N. Strocov, and C. Felser, Science **369**, 179 (2020).

[22] M. Yao, K. Manna, Q. Yang, A. Fedorov, V. Voroshnin, B. Valentin Schwarze, J. Hornung, S. Chattopadhyay, Z. Sun, S. N. Guin, J. Wosnitza, H. Borrmann, C. Shekhar,

N. Kumar, J. Fink, Y. Sun, and C. Felser, Nature Communications **11**, 2033 (2020).
[23] G. Chang, S.-Y. Xu, B. J. Wieder, D. S. Sanchez, S.-M. Huang, I. Belopolski, T.-R. Chang, S. Zhang, A. Bansil, H. Lin, and M. Z. Hasan, Phys. Rev. Lett. **119**, 206401 (2017).
[24] X. Xiao, Y. Jin, D.-S. Ma, W. Kong, J. Fan, R. Wang, and X. Wu, Phys. Rev. B **108**, 075130 (2023).
[25] E. Witten, Riv. Nuovo Cim. **39**, 313 (2016).
[26] K. Hashimoto, T. Kimura, and X. Wu, Progress of Theoretical and Experimental Physics **2017**, 053I01 (2017), [Erratum: PTEP 2019, 029201 (2019)].
[27] B. Seradjeh and M. Vennettilli, Phys. Rev. B **97**, 075132 (2018).
[28] D. Wawrzik, J.-S. You, J. I. Facio, J. van den Brink, and I. Sodemann, Phys. Rev. Lett. **127**, 056601 (2021).
[29] R. Okugawa and S. Murakami, Phys. Rev. B **89**, 235315 (2014).
[30] Y. Liu, J. Lin, V. Wang, and J. Nara, Phys. Scripta **100**, 025939 (2025), arXiv:2107.11044 [cond-mat.mes-hall].
[31] Z. Faraei, T. Farajollahpour, and S. A. Jafari, Phys. Rev. B **98**, 195402 (2018).
[32] S. Juergens and B. Trauzettel, Phys. Rev. B **95**, 085313 (2017).
[33] M. Kharitonov, J.-B. Mayer, and E. M. Hankiewicz, Phys. Rev. Lett. **119**, 266402 (2017).
[34] Z. Zhu, G. W. Winkler, Q. Wu, J. Li, and A. A. Soluyanov, Phys. Rev. X **6**, 031003 (2016).
[35] S. Sekh and I. Mandal, Eur. Phys. J. Plus **137**, 736 (2022).
[36] F. Haidar and I. Mandal, Annals of Physics **478**, 170010 (2025); I. Mandal, arXiv e-prints (2025), arXiv:2505.19636 [cond-mat.mes-hall]; I. Mandal, Phys. Rev. B **111**, 165116 (2025).
[37] Y.-Q. Zhu, D.-W. Zhang, H. Yan, D.-Y. Xing, and S.-L. Zhu, Phys. Rev. A **96**, 033634 (2017).
[38] H. Weng, C. Fang, Z. Fang, and X. Dai, Phys. Rev. B **93**, 241202 (2016).
[39] P. Tang, Q. Zhou, and S.-C. Zhang, Phys. Rev. Lett. **119**, 206402 (2017).
[40] H. Weng, C. Fang, Z. Fang, and X. Dai, Phys. Rev. B **94**, 165201 (2016).
[41] A. Y. Prykhodko, E. V. Gorbar, and P. O. Sukhachov, Journal of Physics: Condensed Matter **37**, 405002 (2025).
[42] G. Chang, S.-Y. Xu, B. J. Wieder, D. S. Sanchez, S.-M. Huang, I. Belopolski, T.-R. Chang, S. Zhang, A. Bansil, H. Lin, and M. Z. Hasan, Phys. Rev. Lett. **119**, 206401 (2017).
[43] G. Xu, H. Weng, Z. Wang, X. Dai, and Z. Fang, Phys. Rev. Lett. **107**, 186806 (2011).
[44] S.-M. Huang, S.-Y. Xu, I. Belopolski, C.-C. Lee, G. Chang, T.-R. Chang, B. Wang, N. Alidoust, G. Bian, M. Neupane, D. Sanchez, H. Zheng, H.-T. Jeng, A. Bansil, T. Neupert, H. Lin, and M. Z. Hasan, Proceedings of the National Academy of Sciences **113**, 1180 (2016).
[45] B. Singh, G. Chang, T.-R. Chang, S.-M. Huang, C. Su, M.-C. Lin, H. Lin, and A. Bansil, Sci. Rep. **8**, 10540 (2018).
[46] L. X. Fu and C. M. Wang, Phys. Rev. B **105**, 035201 (2022).
[47] R. Ghosh and I. Mandal, Physica E: Low-dimensional Systems and Nanostructures **159**, 115914 (2024).
[48] L. Medel, R. Ghosh, A. Martín-Ruiz, and I. Mandal, Sci. Rep. **14**, 21390 (2024); I. Mandal, Annals of Physics **482**, 170181 (2025).
[49] Q. Chen and G. A. Fiete, Phys. Rev. B **93**, 155125 (2016).
[50] Q. Liu and A. Zunger, Phys. Rev. X **7**, 021019 (2017); R. Ghosh and I. Mandal, Journal of Physics: Condensed Matter **36**, 275501 (2024).
[51] T. Zhang, R. Takahashi, C. Fang, and S. Murakami, Phys. Rev. B **102**, 125148 (2020).
[52] C. Cui, X.-P. Li, D.-S. Ma, Z.-M. Yu, and Y. Yao, Phys. Rev. B **104**, 075115 (2021).
[53] L. Luo, W. Deng, Y. Yang, M. Yan, J. Lu, X. Huang, and Z. Liu, Phys. Rev. B **106**, 134108 (2022).
[54] A. Raj, S. Chaudhary, and G. A. Fiete, Phys. Rev. Res. **6**, 013048 (2024).
[55] A. C. Potter, I. Kimchi, and A. Vishwanath, Nature Communications **5**, 5161 (2014); Y. Zhang, D. Bulmash, P. Hosur, A. C. Potter, and A. Vishwanath, Sci. Rep. **6**, 23741 (2016).